

Efficient Utilization of Rare Earth Permanent-Magnet Materials and Torque Ripple Reduction in Interior Permanent-Magnet Machines

Zhentao S. Du, *Student Member, IEEE*, and Thomas A. Lipo, *Life Fellow, IEEE*

Abstract—This paper proposes a new interior permanent-magnet machine (IPMM) design in which the rotor consists of several rotor segments arranged in the axial direction, aiming to improve the utilization of rare earth permanent-magnet (PM) materials and reduce the torque ripple. The proposed design is optimized to feature a 21% reduction of rare earth PM materials and a 50% reduction of ripple torque ratio compared with the Camry 2007 design, which uses the conventional pole-shaping technique to suppress its torque ripple. Although the torque is reduced by 9%, the torque per magnet weight is improved by 15%, indicating the PMs are more efficiently used in the proposed design. The designs are verified by 3-D finite element. Despite the small torque reduction, the efficiency of the proposed design is still about the same as the Camry design.

Index Terms—Cogging torque, differential evolution, efficiency, finite-element (FE) modelings, interior permanent-magnet machines (IPMMs), optimization, ripple torque, 3-D machine design.

I. INTRODUCTION

INTERIOR permanent-magnet machines (IPMMs) are widely used in many industrial applications due to their high torque density and efficiency. IPMMs are also important in traction applications in which torque density is the primary metric. The main drawback of IPMMs is their use of expensive rare earth permanent magnets (PMs). Their cost is still a major concern due to the shortage of rare earth materials around the world.

Many alternative designs promote rare earth PM reduction. The third-generation Toyota Prius uses less amount of rare earth PMs than previous generations to produce the same output power at an increased speed [1]. Many researchers strive for other rare-earth-free designs. The switched reluctance machine is one candidate [2]. However, it suffers from poor torque density. The ferrite PM-assisted synchronous reluctance machine (PMASRM) is another option [3]. Its torque density is still

much lower than that of the IPMMs [3]. Therefore, poor torque density remains the primary issue with rare-earth-free designs.

IPMMs have large pulsating torque due to their reaction and reluctance torques [4]. Using an odd number of stator slots per pole pairs can effectively reduce the pulsating torque [5]. Skewing the rotor is also a common technique to reduce torque ripple. However, skewing has been proven to be ineffective when the stator iron is saturated [6]. Pole shaping is yet another common technique to minimize the torque ripple [7] where the pole face is shaped radially to produce a sinusoidal air-gap permeance. However, pole shaping becomes very difficult in IPMMs where flux barriers and PM flux concentration are present. Other alternatives are shaping the PM flux in the axial direction [8] and manipulating the flux barriers using different rotor modules in the axial direction [9], [10]. These methods show promising results since they use an extra degree of freedom to reduce the distortion of PM flux linkage.

This paper proposes a new design concept consisting of the use of a small number of rotor segments arranged in the axial direction. The design is optimized to reduce the utilization of rare earth PM materials and the pulsating torque while sacrificing only a small amount of torque density. In contrast, the conventional pole shaping technique is also shown to be ineffective in V-shape IPMMs with PM flux concentration. The proposed design concept saves 21% rare earth PM materials for 9% average torque reduction and reduces the torque ripple ratio by 50% at rated load with saturated back iron. The rare earth materials are more efficiently used since the torque per magnet weight is improved by 15%. Thus, the PM cost reduction is potentially considerable.

II. PROPOSED DESIGN CONCEPT

The Camry 2007 model (Camry) is an optimized V-shape IPMM design in which a pole shaping technique is applied to purposefully reduce the pulsating torque. The Camry design is shown in Fig. 1(a) with two rotor notches on the rotor surface as indicated in Fig. 1(b). The rotor notches suppress some of the spatial harmonics in the PM flux distribution and subsequently reduce the mutual couplings between the harmonics of the magnetic loading and the electric loading in the air gap.

The proposed design concept [11] is also based on the concept of utilizing rotor notches employed on the rotor surface. Here, the rotor is divided into several segments in the axial direction.

Manuscript received October 21, 2016; revised January 11, 2017; accepted March 5, 2017. Date of publication March 27, 2017; date of current version July 15, 2017. Paper 2016-EMC-1027.R1, presented at the 2015 IEEE Energy Conversion Congress and Exposition, Montreal, QC, Canada, Sep. 20–24, and approved for publication in the IEEE TRANSACTIONS ON INDUSTRY APPLICATIONS by the Electric Machines Committee of the IEEE Industry Applications Society. (*Corresponding author:* Zhentao S. Du.)

The authors are with the Wisconsin Electric Machines and Power Electronics Consortium, Department of Electrical and Computer Engineering, University of Wisconsin–Madison, Madison, WI 53706 USA (e-mail: zd4@wisc.edu; lipo@engr.wisc.edu).

Color versions of one or more of the figures in this paper are available online at <http://ieeexplore.ieee.org>.

Digital Object Identifier 10.1109/TIA.2017.2687879

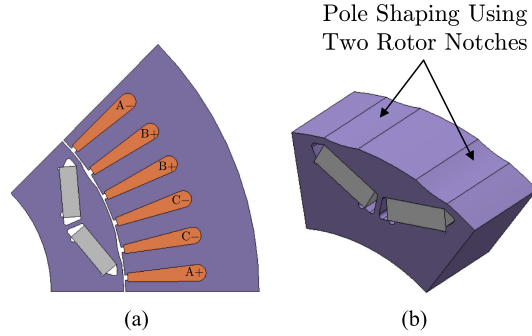


Fig. 1. Camry 2007 IPMM model: (a) winding sequence; and (b) pole shaping applied on the rotor surface.

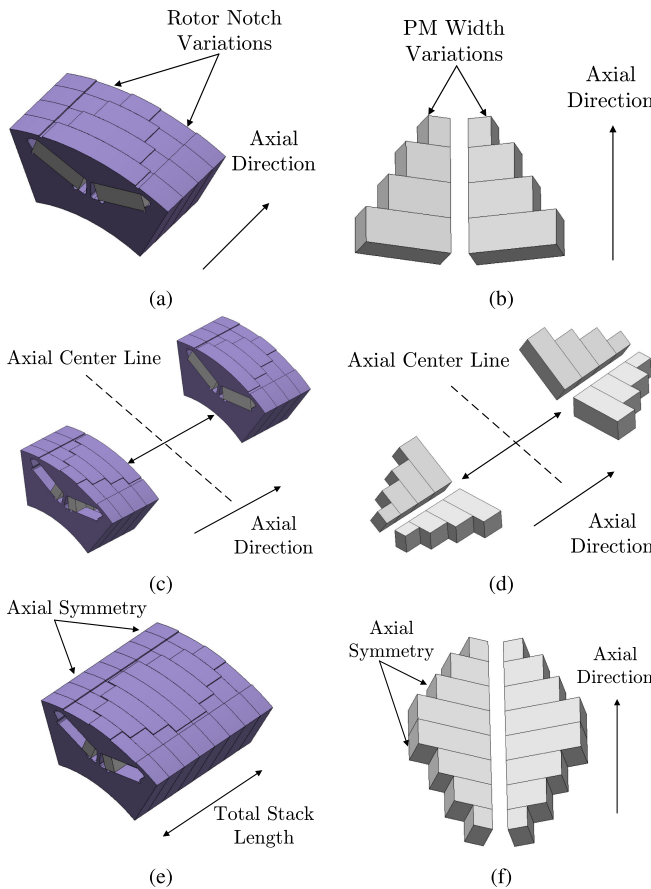


Fig. 2. Proposed design concept: (a) notch variations; (b) PM variations; (c) two identical rotor modules stacked back-to-back in the axial direction; (d) PMs also stacked back-to-back in the axial direction; (e) overall rotor design; and (f) overall PM arrangement.

In each segment, the pitch of the notches and the width of PMs are free to vary as shown in Fig. 2(a) and (b), aiming to further reduce the pulsating torque. The thickness of the PMs is selected as the same as that of the PMs in Camry so that they are capable of withstanding the same amount of demagnetization fields. To eliminate the unbalanced axial force acting on the shaft, an identical rotor module is added and the two rotor modules with identical rotor segments are placed back-to-back along the axial direction as illustrated in Fig. 2(c) and (d). The additional rotor

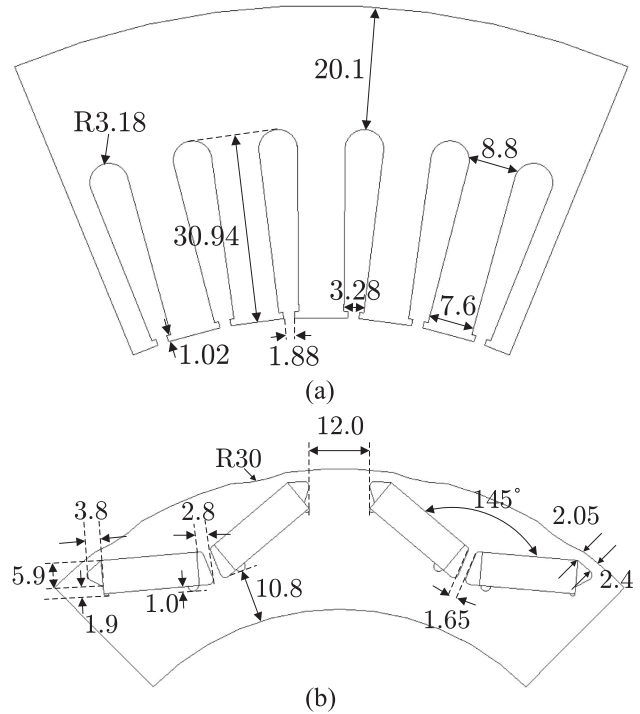


Fig. 3. Dimensions (in millimetres unless specified otherwise) of Camry 2007 design: (a) stator dimensions; and (b) rotor dimensions [12].

module creates axial symmetry as depicted in Fig. 2(e) and (f). The PM cavities are purposely kept the same throughout all the rotor segments to prevent short-circuited magnetic fields from existing between any two adjacent segments in the axial direction. Inexpensive glass or plastic spacers are required to secure the short-pitched PMs in the PM cavities. The stator iron and the windings of the proposed design are chosen to be exactly the same as those of the Camry so that a fair comparison can be made. All the dimensions of the Camry design are shown in Fig. 3 [12]. The key geometric parameters of the Camry [12] are compared against those of the proposed design in Table I.

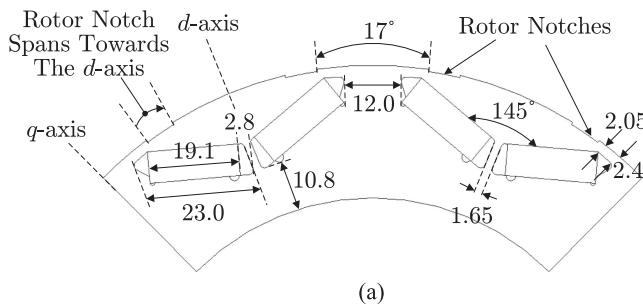
III. DESIGN CONSIDERATIONS

The proposed design concept basically modifies the rotor of the Camry design in the axial direction. Two rotor designs are developed here by applying the proposed design concept as illustrated in Fig. 2. The aim is to compare their performance against the Camry design. The two rotor designs and dimensions are illustrated in Fig. 4. The first rotor design, denoted as Design I (D-I), uses the exact same PM cavity design as that of the Camry design. The only difference between D-I and the Camry design is the size of the rotor notches, which are made on top of the rotor lamination, as illustrated in Fig. 4(a). The rotor notch starts to span above the PMs at 8.5° away from the q -axis. The maximum width of the PMs in D-I is exactly the same as that of the Camry design.

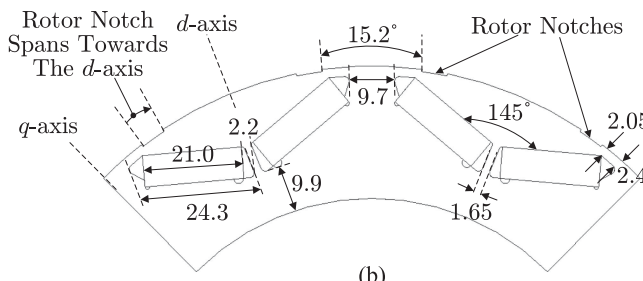
In contrast, the second rotor design, denoted as Design II (D-II), has a slightly different PM cavity design. The entire V-structure is moved inward and the length of the V-structure arm is increased slightly so that the maximum width of the

TABLE I
KEY PARAMETERS OF CAMRY AND PROPOSED DESIGN

	Camry IPMM	Proposed Design
Stator outer diameter (OD) [mm]	264	264
Stator inner diameter (ID) [mm]	161.93	161.93
Rotor outer diameter (OD) [mm]	160.47	160.47
Rotor inner diameter (ID) [mm]	105	105
Active stack length l [mm]	61	sum to 61
Air gap thickness g [mm]	0.73	0.73
Slot pitch τ_s [mech. °]	7.5	7.5
Tooth width/depth t_{ts}/d_{ls} [mm]	7.6/30.94	7.6/30.94
PM thickness d_{pm} [mm]	6.6	6.6
PM width w_{pm} [mm]	19.1	vary
PM length l_{pm} [mm]	61	sum to 61
Center pose thickness d_{cp} [mm]	1.65	1.65
Min. bridge thickness d_{bg} [mm]	2.05	2.05
V-shape angle α_v [°]	145	145
Poles/slot per pole per phase P/q	8/2	8/2
Turns per slot/no. of circuits	14/2	14/2
Rotor speed ω_{rm} [rpm]	2800	2800
Current density J [A/mm²]	19	19
Current per phase peak [A]	276	276
Current angle γ [°]	50	50



(a)



(b)

Fig. 4. Proposed rotor lamination designs and dimensions (in millimetres unless specified otherwise) of: (a) D-I; and (b) D-II (The PM width is at maximum in each rotor lamination).

PMs in D-II is slightly increased, as illustrated in Fig. 4(b). The increased PM cavity enables the rotor segment to contain more PM content. However, the increased PM cavity need not be fully filled according to the proposed design concept. In D-II, the rotor notch starts to span above the PMs at 7.6° away from the q -axis. The rib becomes narrower in D-II due to the increased PM cavity. The rotor bridges remain intact in both rotor designs. The key rotor parameters of both designs are defined in Fig. 5(a) and compared against the Camry design in Table II. It should be noted that the rotor notches in Camry are smooth curves, whereas in the proposed designs, the rotor

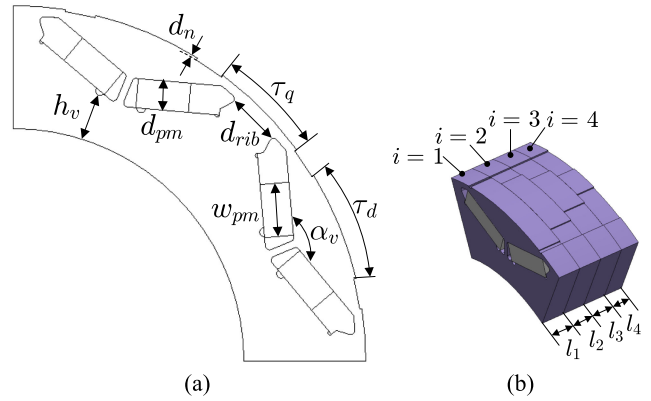


Fig. 5. Key geometric parameters: (a) parameters of a segment in the radial plane; and (b) parameters in the axial plane for four rotor segments.

TABLE II
KEY ROTOR DESIGN PARAMETERS

	Camry	D-I	D-II
V-shape angle α_v [°]	145	145	145
q -axis pole arc τ_q [°]	17	17	15.2
d -axis pole arc τ_d [°]	13.8	vary	vary
Rib thickness d_{rib} [mm]	12	12	9.7
V-cavity height h_v [mm]	10.8	10.8	9.9
PM thickness d_{pm} [mm]	6.6	6.6	6.6

TABLE III
ROTOR DESIGN VARIABLES

	D-I		D-II	
	Min.	Max.	Min.	Max.
d -axis pole arc τ_{di} [°]	1	28	1	29.8
PM width w_{pmi} [mm]	1	19.1	1	21
Notch depth d_{ni} [mm]	0.1	0.5	0.1	0.5
Segment length l_i [mm]	1	30.5	1	30.5

notch has uniform depth throughout the span of the notch, as illustrated in Figs. 3(b) and 4.

In each rotor design, the width of the PMs, the pitch and depth of the rotor notches, and the stack length are the geometric variables that are free to vary. Each rotor design has several rotor segments, as shown in Fig. 5(b), where i will be used to designate the rotor segment number. The design variables are varied in each rotor segment to improve the performance of each rotor design. An optimization routine is used to search for feasible candidates in the search space spanned by the geometric variables. The boundary of the search space is governed by the limits of all the geometric variables, which are also provided in Table III. These geometric limits will be used in the optimization as the boundary constraints.

IV. OPTIMIZATION FORMULATION

The geometric variables of each rotor segment are determined by finite-element (FE)-based differential evolution (DE). The DE algorithm interfaces with a FE program to acquire the per-

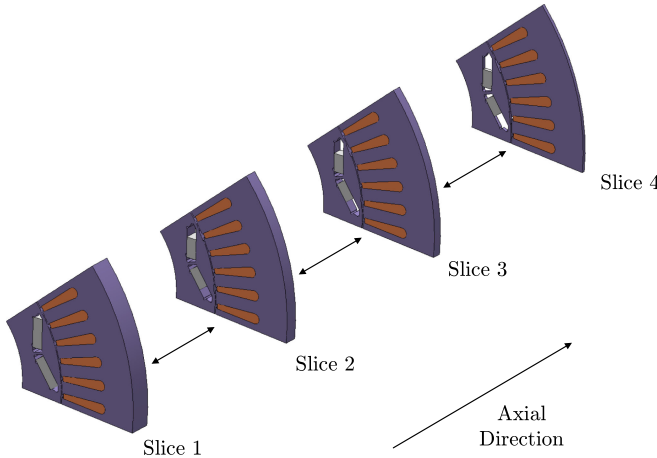


Fig. 6. Multislices for the proposed design concept.

formance of a design candidate. 3-D FE analysis is normally required for simulating geometric variations in both the radial and axial directions. In this case, the multislice method [13] is used in the optimization instead of the computationally intensive 3-D FE-based optimization because axial symmetry still exists within each rotor segment. The stator is also divided accordingly into segments so that each stator segment has the exact length of the corresponding rotor segment. Each pair of stator and rotor segments forms a 2-D FE slice as shown in Fig 6. The 2-D-transient FE method is performed to obtain the instantaneous torque produced by each slice. The resultant torque of the entire rotor unit is the vector sum of the torque contributed by all the slices.

The main design objectives are the minimization of both pulsating torque and rare earth magnet usage. The torque density is also important. The torque per magnet weight, defined as the PM utilization factor (*PMUF*), can measure the efficiency of using PMs in a design. It is preferable to solve the design problem using multiobjective optimization [14]. Since the design objectives are conflicting in this case, a single optimum solution cannot be easily defined [15]. The DE adopts the Pareto-dominance selection process. The candidates that are not dominant trace a Pareto-front in the objective space, which is a set of the best compromise or Pareto-optimal solutions [15]. The optimization minimizes the three objective functions

$$\text{obj}_1 = T_{\text{err}} = (T_{e\max} - T_{e\min})/T_{e\text{avg}} \quad (1)$$

$$\text{obj}_2 = 1/T_e \quad (2)$$

$$\text{obj}_3 = 1/\text{PMUF} = m_{\text{pm}}/T_e \quad (3)$$

where T_{err} denotes torque ripple ratio, T_e denotes torque, and m_{pm} is the mass of the PMs.

The optimization is subject to a number of constraints. The geometric bounds, as identified in Table III, are the boundary constraints of the optimization. The second constraint is an equality constraint ensuring that the total length of all the rotor

TABLE IV
SETTINGS OF THE DE ALGORITHM FOR D-I AND D-II

	$i = 2$	$i = 3$	$i = 4$
Number of population members N_p	30	50	70
Number of generations g_{\max}	50	50	50
Total populations P_{tot}	1500	2500	3500
Mutation weighting factor F	0.8	0.8	0.8
Crossover probability C_r	0.9	0.9	0.9

segments equals the original stack length

$$\sum_i l_i = 0.5l. \quad (4)$$

The factor 0.5 is applied in (4) because the optimization only needs to account for one rotor module due to axial symmetry. It is best to handle (4) by eliminating a length variable in the objective function. The third constraint is the inequality constraint ensuring all candidates satisfy the torque requirement

$$\sum_i T_{ei} \geq T_e^{\text{req}} \quad (5)$$

where T_e^{req} denotes the torque requirement.

The optimization follows initialization, mutation, crossover, and selection to develop new generations [15]. The differential variation method [15] is used for mutation. Other parameters for the algorithm are provided in Table IV. The number of members becomes larger as the number of segments increases, because larger number of rotor segments have more design variables involved. The torque of each candidate is evaluated at the maximum torque per ampere (MTPA).

V. OPTIMIZATION OUTCOMES AND DISCUSSIONS

The 2-D FE-based DE searches for feasible designs in the search space of which dimensions are determined by the number of design variables. After many trial runs, it was found that the *d*-axis pole arc (τ_d) can be set to vary proportionally with the width of the PMs (w_{pm}), and that the depth of the notches (d_n) can be fixed at its boundary value in each rotor segment, since the optimization always approaches designs with these characteristics. Taking these steps can reduce the number of design variables and improve the accuracy of the DE search algorithm.

For the case of two rotor segments, the performance of the design candidates are shown in Fig. 7 for the case when the torque constraints are not imposed in both designs. The approximate Pareto-fronts are also indicated in Fig. 7(a) and (b), which clearly illustrate the design tradeoffs. In Fig. 7, the *PMUF* in both designs is inversely proportional to the torque of the machine. Although the torque decreases as the PM content decreases, the PM content always decreases faster than the total torque, since the design still retains a large amount of reluctance torque. The *PMUF* is very large in the candidate designs that use a small amount of PM material. However, the torque produced by these candidate designs is much less than the torque

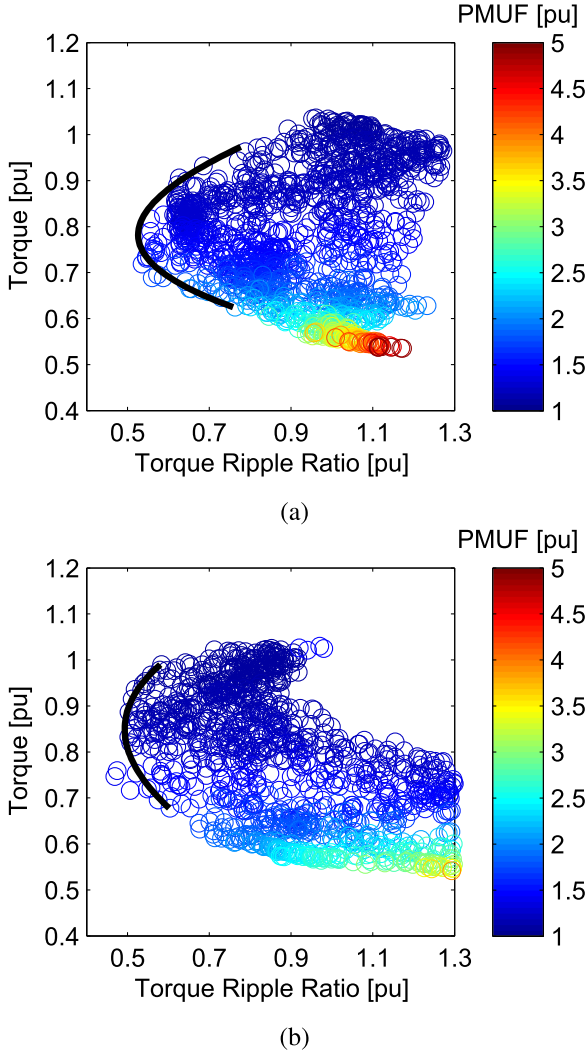


Fig. 7. Scatter plots of feasible design candidates for the case of two rotor segments in the objective space (base values: Camry's rated performance per pole per module: torque ripple ratio: 18%, torque: 14.5 Nm, and PMUF: 0.25 Nm/g): (a) D-I; and (b) D-II (Solid lines are the approximate Pareto-fronts).

produced by candidate designs that have a larger amount of PM material.

The result also suggests that the proposed designs need to sacrifice torque or torque density for the reduction of the PMs. Along the Pareto-fronts of both designs, the torque ripple ratio reduces significantly as the torque and the magnet content decrease, but the torque ripple ratio actually increases again after removing too much magnet content, in which case the designs approach features of a synchronous reluctance machine. Although the PMUF can be improved dramatically, the torque and the pulsating torque are both in unfavorable directions in these designs.

The approximate Pareto-fronts are illustrated in Fig. 8(a) and (b) for the cases of up to four rotor segments in both designs. These figures show that increasing the number of rotor segments can further reduce the pulsating torque. However, the pulsating torque shows only a small reduction beyond the design with two rotor segments. In fact, two rotor segments has already shown

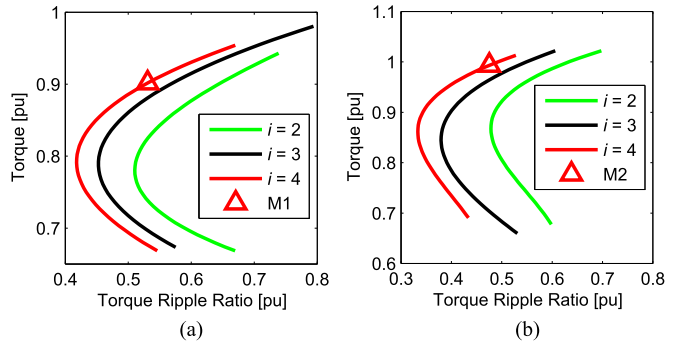


Fig. 8. Collections of the approximate Pareto-fronts for up to four rotor segments: (a) D-I; and (b) D-II.

TABLE V
DIMENSIONS OF OPTIMUM DESIGNS WITH FOUR SEGMENTS

Design M1	$i = 1$	$i = 2$	$i = 3$	$i = 4$
PM width w_{pmi} [mm]	19.1	13.6	12.1	11.7
d -axis pole arc τ_{di} [$^\circ$]	28	20.4	18.4	17.8
Segment length l_i [mm]	12.5	4.8	12	1.2
Notch depth d_n [mm]	0.5	0.5	0.5	0.5
q -axis pole arc τ_{qi} [$^\circ$]	17	17	17	17
Design M2	$i = 1$	$i = 2$	$i = 3$	$i = 4$
PM width w_{pmi} [mm]	21	19.3	15.2	13.1
d -axis pole arc τ_{di} [$^\circ$]	29.8	27.6	22	19.2
Segment length l_i [mm]	15.1	7.2	6.8	1.4
Notch depth d_n [mm]	0.5	0.5	0.5	0.5
q -axis pole arc τ_{qi} [$^\circ$]	15.2	15.2	15.2	15.2

significant improvement. In addition, increasing the number of rotor segments clearly increases the manufacturing cost. Therefore, the optimization stops at the case of four rotor segments. Two segments can be adopted if manufacturing cost is a concern.

In summary, both designs need to sacrifice excessive amount of torque or torque density for the minimum pulsating torque, making the proposed designs less torque dense. To avoid losing too much torque, the torque requirement is selected to be 90% of the Camry's for D-I. In that manner, the proposed design is optimized to use PMs more efficiently without compromising too much torque or torque density, while the pulsating torque can still be reduced significantly. For D-II, since the design increases the PM capacity, the design is capable of reducing the pulsating torque without sacrificing any torque or torque density. Thus, the torque requirement is set to 100% of the Camry.

The optimization was rerun for both designs incorporating the torque constraints. The optimum designs for four rotor segments are indicated in Fig. 8(a) and (b) as "M1" and "M2." The optimum designs and dimensions are summarized in Table V and illustrated in Fig. 9. If the full pitch PM maps to 180 electrical deg., then the projected PM shapes can be plotted in Fig. 10(a) and (b). The PM shapes mainly trace a fundamental plus a third harmonic shape in both designs. As indicated in Fig. 10(c), the PM shape in M2 shows a higher fundamental and third harmonic because M2 uses more PMs to match the torque of Camry. The d -axis pole arcs (τ_d) follow the same shapes according to this mapping since they are proportional to the widths of the PMs.

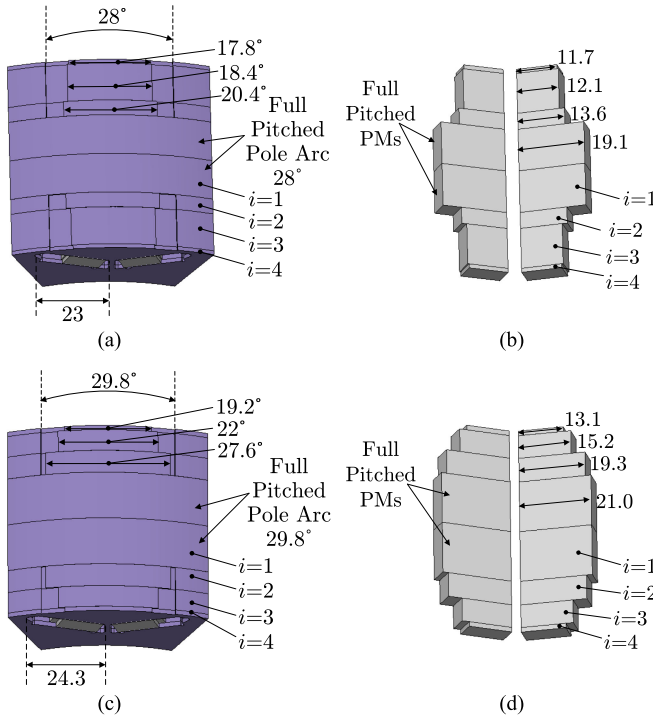


Fig. 9. Final proposed designs with key dimensions (in millimetres unless specified otherwise): (a) rotor of M1; (b) PMs of M1; (c) rotor of M2; and (d) PMs of M2 (other dimensions can be found in Table V and Fig. 4).

VI. PERFORMANCE COMPARISONS

The performance of the final designs M1 and M2 are compared against that of the Camry model in this section. The no-load and rated-load flux density distributions of the Camry model are illustrated in Fig. 11. Fig. 11(a) shows that the PM flux is concentrated along the d -axis due to the effect of the rotor notches and the V-shape angle. The back iron is just becoming saturated when the rated current is applied as indicated in Fig. 11(b). The saturation in the back iron further distorts the PM flux linkage and produces additional pulsating torque. The teeth are usually saturated for designs which efficiently utilize the stator space to accommodate both the copper and the iron.

For purposes of comparison, 3-D FE models were constructed for the Camry and the proposed designs. The 3-D no-load flux density distributions for all the designs are illustrated in Fig. 12. The pole shaping technique used in the Camry design shows a flux concentration around the center of the pole in the air gap but shows a uniform distribution along the axial direction, as depicted in Fig. 12(a), and the PMs have uniform flux density distribution at no load as illustrated in Fig. 12(b). Both M1 and M2 show flux concentration variations in the radial and axial directions as shown in Fig. 12(c) and (e). The shapes of the flux density distribution in the air gap are similar to the PM shapes of M1 and M2 illustrated in Fig. 10(a) and (b). The extra degree of freedom in the axial direction allow the proposed designs to shape the PM flux linking the stator coils more accurately and effectively than in the Camry design. The flux density in the proposed magnet configurations are also uniformly distributed at no load, as clearly indicated in Fig. 12(d) and (f). The uniform

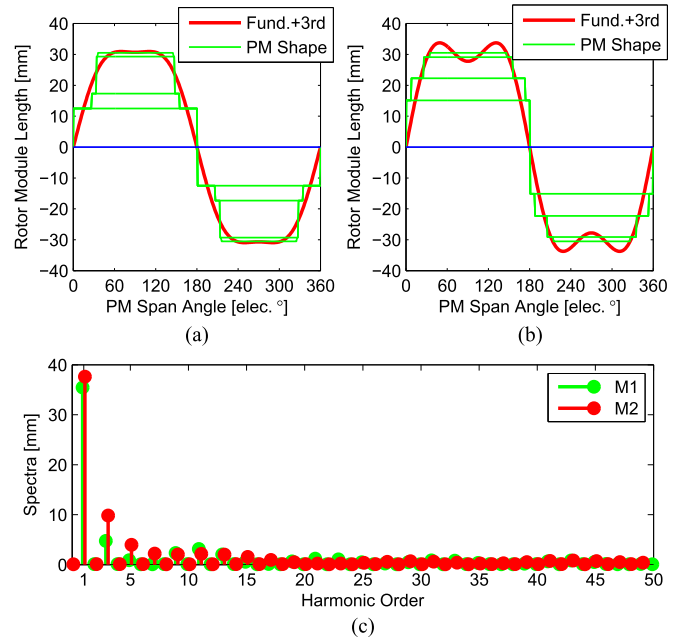


Fig. 10. Proposed PM configurations (negative length means the opposite pole): (a) PM shape of M1; (b) PM shape of M2; and (c) PM shape spectra of M1 and M2.

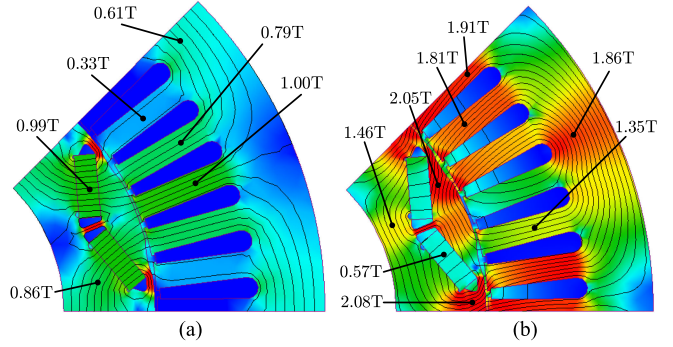


Fig. 11. Camry's flux density distributions: (a) no load; and (b) rated load at MTPA.

flux density of the PMs ensures that the PM flux still traverses radially rather than axially, which would otherwise result in higher eddy current loss in the conventional laminations.

The back-electromotive forces (EMFs) of the Camry design, M1, and M2 are given in Fig. 13. The back-EMFs computed by the 2-D multislice method closely match the back-EMFs computed by the 3D FE method for all the designs. M1 has smallest back-EMF due to its reduced amount of PM materials. The fundamental component of M2 is the same as that of the Camry as shown in Fig. 13(d) since M2 actually uses the same amount of PM materials as the Camry. Although the pole shaping technique is employed in Camry design, the back-EMF shows some residues of the 5th and 7th harmonics and much higher 11th and 13th harmonics than those of the proposed designs. The spectral analysis suggests that the pole shaping technique used in the Camry cannot perfectly remove

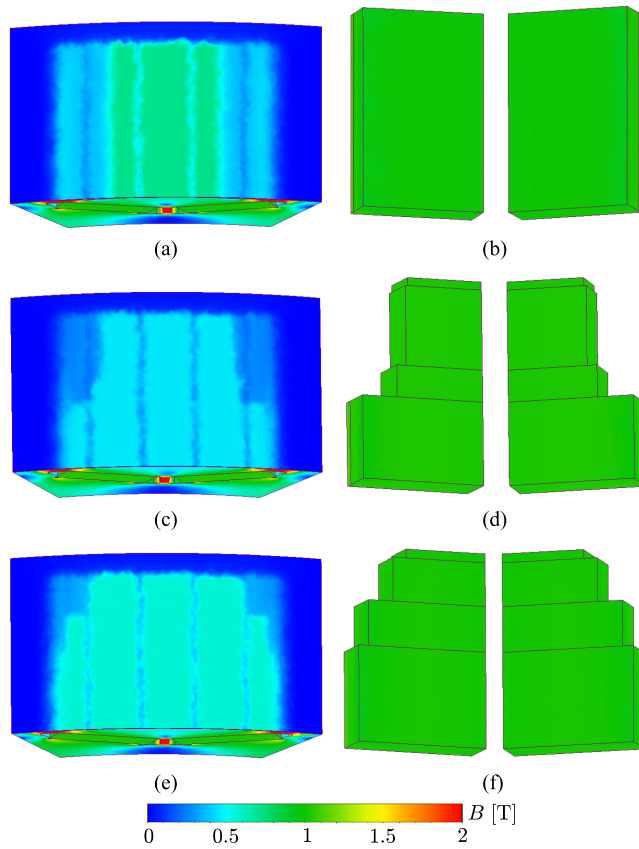


Fig. 12. 3-D no-load flux density distributions in: (a) air gap of Camry; (b) PMs of Camry; (c) air gap of M1; (d) PMs of M1; (e) air gap of M2; and (f) PMs of M2.

all the harmonics in the back-EMF, especially the 11th and 13th harmonics.

The ripple torque of PM machines is essentially caused by interactions between the stator and rotor magnetomotive force (MMF) harmonics in the air gap [5]. The harmonics in the back-EMFs suggest the same order of spatial harmonics exist in the spatial PM flux distributions and the rotor MMFs in the air gap. These spatial harmonics couple with those of the stator MMF to produce harmonic ripple torques. However, only the stator and rotor MMF harmonics with the same spatial frequencies can contribute to the ripple torque, because the magnetic field energy is a spatial integral of the product of the stator and rotor MMF harmonics [5]. Since the 5th spatial harmonic of the stator and rotor MMF rotate at ω_e and $5\omega_e$, respectively, they combine to produce the 6th harmonic ripple torque; the 7th spatial harmonics of the stator and rotor MMFs rotate at $-\omega_e$ and $7\omega_e$, respectively, they also combine to produce the 6th harmonic ripple torque [5]. In the same manner, the 11th and 13th stator and rotor MMF harmonics produce the 12th harmonic ripple torque. The stator MMF does not contain any triplen harmonics because of the floating neutral; for this reason, the harmonic order of ripple torques is always a multiple of six. Refer to Fig. 13(d), the Camry design indicates higher 5th, 7th, 11th, and 13th harmonics, which suggests that the Camry design

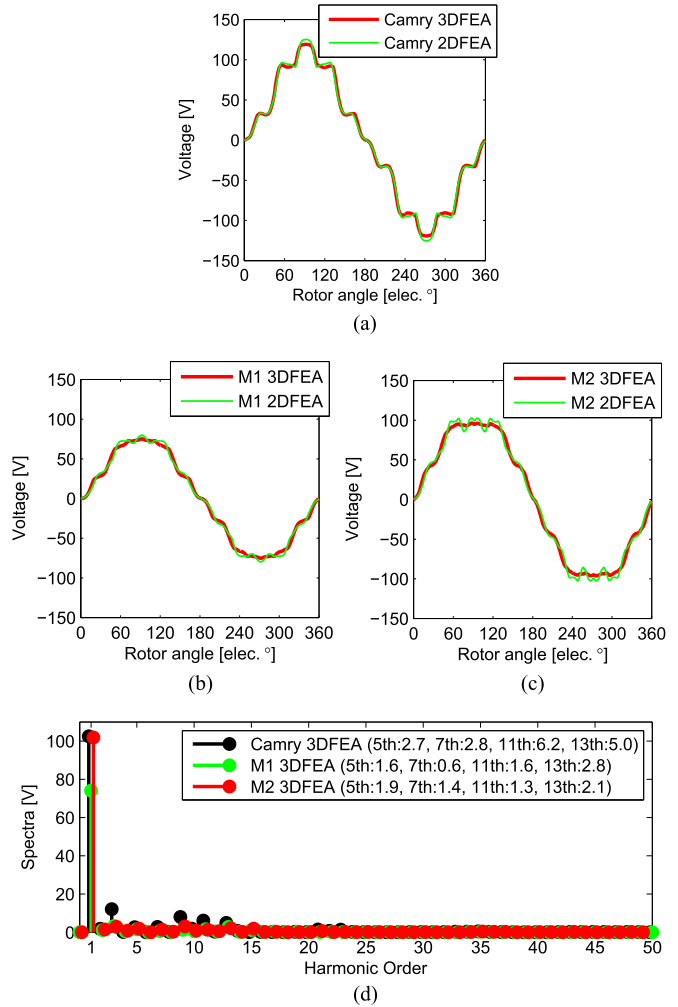


Fig. 13. Back-EMFs and corresponding spectra of all the designs at rated speed (one electrical period): (a) Camry; (b) M1; (c) M2; and (d) spectra of all three designs.

produces higher 6th and 12th harmonic ripple torques than the proposed designs.

The cogging torques of all three designs are shown in Fig. 14. The cogging torques obtained by the 2-D multislice method shows small difference compared to the results computed by the 3-D FE method. The small difference is mainly caused by the end effects, which are included in the 3-D FE model but not in the 2-D FE model. The smaller cogging torque indicated in the 3-D FE results suggests small PM flux leakage existed on both ends of the machine. The cogging torques of M1 and M2 are smaller than that of the Camry design using pole shaping. Thus, the spectra of the Camry's cogging torque are higher than those of the proposed designs as illustrated in Fig. 14(d).

The cogging torque behavior of IPMMs can be explained by the model used in [16]. In IPMMs, when a slot opening enters the magnet pole arc, the magnetic field energy increases, resulting in a negative torque pulse; when a slot opening leaves the pole arc, the magnetic field energy decreases, resulting in a positive torque pulse. The change of magnetic field energy is

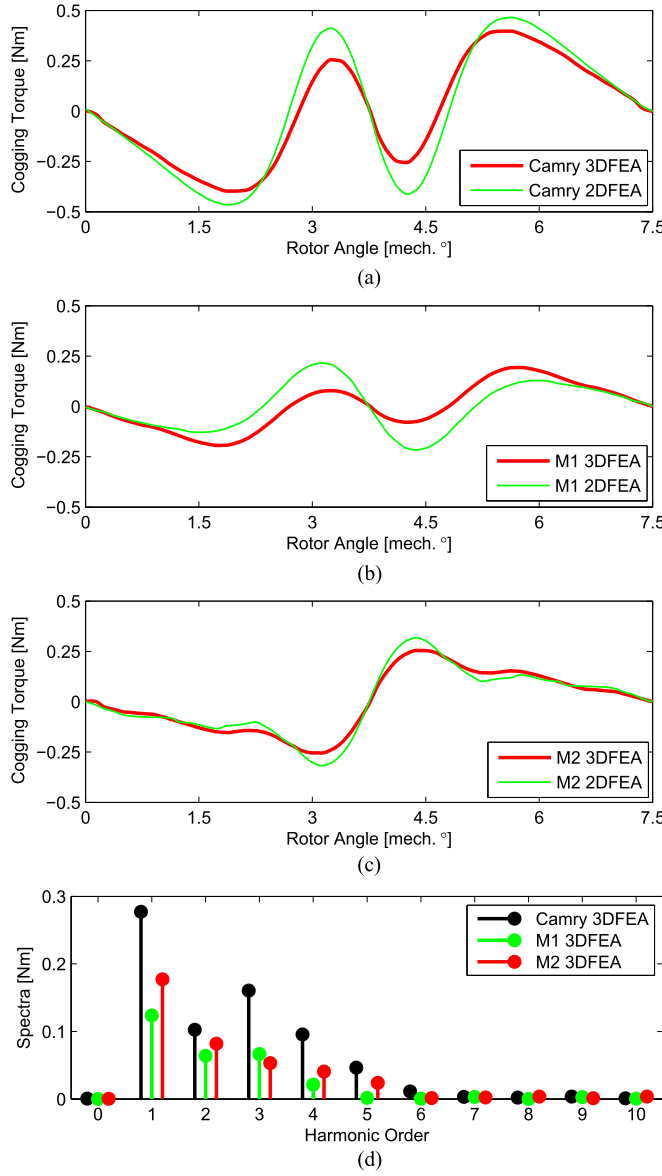


Fig. 14. Cogging torques and corresponding spectra over one slot pitch rotation of all the designs: (a) Camry; (b) M1; (c) M2; and (d) spectra of all three designs.

zero when the slot openings are within the pole arcs. The torque pulse reaches the maximum magnitude when a pole arc edge is near the slot. The pole arcs and their edges are shown in Fig. 15. The magnitude of the torque pulse is determined by the tooth width. Large tooth width or small slot width can reduce the magnitude of the torque pulse. Moreover, when the PMs are full pitched, although most of the flux is focused within the short-pitched pole arc, as illustrated in Fig. 15(b), there still exists a nonnegligible amount of flux flowing across the rotor notches. In this case, the effect of the rotor notches cannot be neglected. The magnetic field energy increases when the rotor notches align with the teeth resulting in a negative torque pulse, and the magnetic field energy decreases when the rotor notches misalign with the teeth, resulting in a positive torque pulse. Furthermore, the fundamental period of the cogging torque over one slot

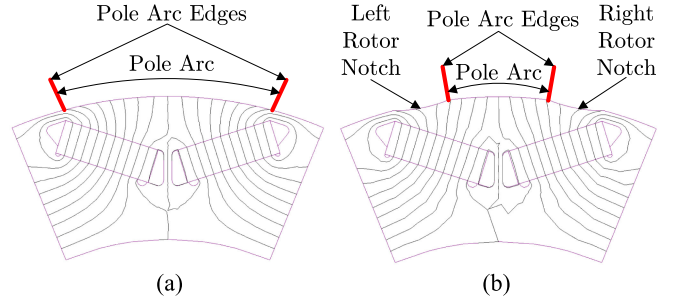


Fig. 15. Illustrations of pole arcs and their edges in the Camry design: (a) full-pitched pole arc without rotor notches; and (b) short-pitched pole arc with rotor notches.

pitch rotation can be obtained using the slot pitch divided by a factor N_p [16]. In these designs, N_p is unity, and therefore, the fundamental cogging torque period is exactly one slot pitch, as shown in Fig. 14.

The cogging torque waveform of the Camry design shows several torque pulses over a slot pitch rotation, as shown in Fig. 14(a). In this design, the PM is full pitched and the PM flux flows through the rotor notches. Thus, the effect of the rotor notches are not negligible. When the rotor notches begin to align with the teeth, the cogging torque shows a negative torque pulse. Next, a slot opening leaves the pole arc, resulting in the second positive torque pulse. Then, a slot opening enters the pole arc, which produces the third negative torque pulse. After a half slot pitch rotation, the rotor notches begin to misalign with the teeth. Therefore, the cogging torque shows a final positive torque pulse at the end of the rotation.

In contrast, the rotor notches have little impact on the cogging torques of M1 and M2 because of the short-pitched PMs used in the rotor segments with short-pitched pole arcs. The PM flux is mainly focused within the pole arcs. The cogging torque of each rotor segment in M1 and M2 is shown in Fig. 16. Except for $i = 2$ of M1 showing two small torque pulses near the half slot pitch, which are caused by the rotor notches, the other cogging torque pulses are mainly due to the change of magnetic field energy due to the slot openings. The resultant total cogging torque of M1 has several oscillations because the torque pulses occur in different rotor positions, as shown in Fig. 16(a).

In M2, since the two major torque pulses are out of phase as shown in Fig. 16(b), the total cogging torque is greatly reduced with fewer oscillations. It is important to point out that the cogging torque produced by the third rotor segment ($i = 3$) in M2 is very small given the large amount of PM material used in this rotor segment, since the pole arc pitch of this rotor segment is roughly three slot pitches. When the pole arc is a multiple of slot pitch, there is always a slot opening entering on one side of the pole arc while another slot opening is leaving on the other side, resulting in torque pulse cancellation. Although the first rotor segment ($i = 1$) of both designs has full-pitched pole arcs without rotor notches and full-pitched PMs [i.e., the case shown in Fig. 15(a)], the torque pulses in M2 exhibit opposite polarity compared to M1. The reason is because of the longer pole pitch

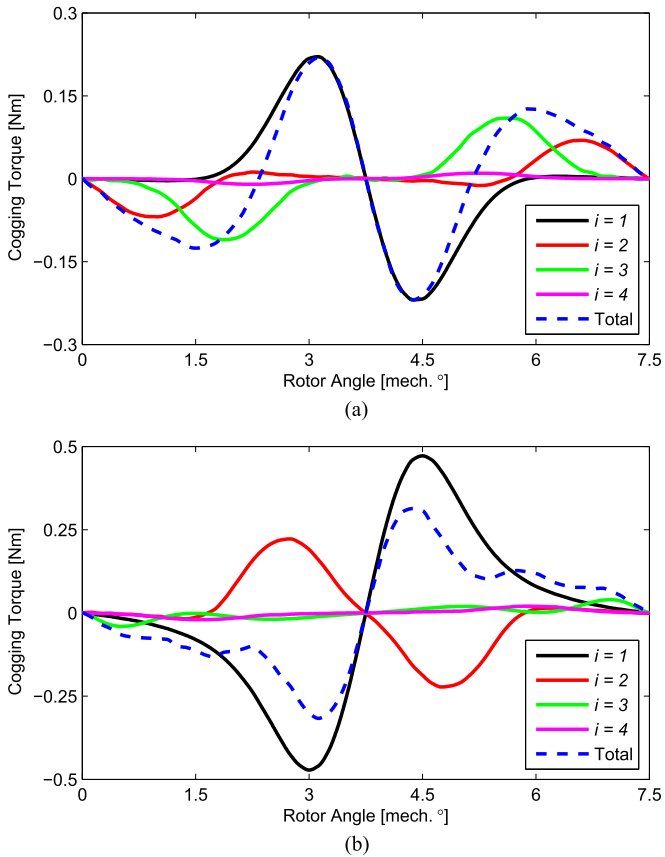


Fig. 16. Cogging torques over a slot pitch rotation of each rotor segment: (a) M1; and (b) M2.

in M2, which changes the order how the slot openings enter and leave the pole arc.

All the designs are driven by the rated current at rated speed and tuned to the MTPA operating point. The total instantaneous torques of all three designs are provided in Fig. 17. Again, the dynamic torques obtained by the 2-D multislice method match very well with the results computed by the 3-D FE method. The very small difference between the two methods also suggests that the proposed designs have little end effects. As shown in Fig. 17(d), the Camry model shows higher 6th and 12th harmonics than the proposed designs because of the 5th, 7th, 11th, and 13th harmonics in the PM flux linkage. The proposed design shows much less pulsating torque since they mainly suppress the 11th and 13th harmonics as demonstrated in Fig. 13(d). Although M2 has more PM materials than M1, the pulsating torque is even a little smaller than that of M1. It suggests that making modification of the rib thickness d_{rib} also helps reduce the pulsating torque. The remaining pulsating torque is mainly caused by the reluctance torque component.

All the 3-D FE results are summarized in Table VI. M1 reduces rare earth PM materials by 21%, and hence, it lowers the PM cost by 21%, which is considerable, especially when the rare earth PMs are very expensive. M1 also uses the PM more efficiently since its $PMUF$ is 15% higher than that of the Camry design. M1 has only as small as 9% torque reduction. Both M1 and M2 achieve smaller cogging torque and pulsat-

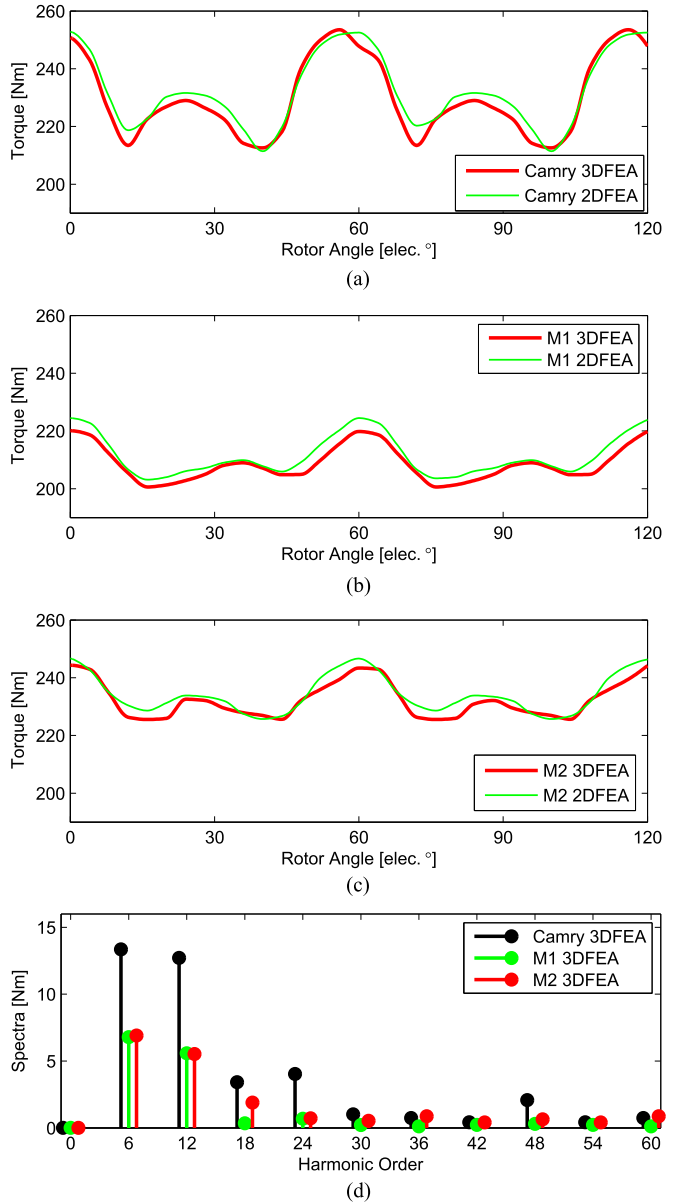


Fig. 17. Instantaneous torque and corresponding pulsating torque spectra of all the designs driven by the rated current at rated speed and MTPA (two pulsating torque periods): (a) Camry; (b) M1; (c) M2; and (d) spectra of all three designs.

ing torque than those of the Camry design, as summarized in Table VI. The reason is that the proposed design concept is more effective in suppressing the harmonic distortions in the PM flux linkage, as supported by the back-EMF total harmonic distortions (THDs) in Table VI. In essence, the Camry design inefficiently adds another 21% of rare earth PMs for an extra 9% torque production with more than 50% extra pulsating torque. M2 is unable to save any PM materials because it is designed to match the torque capability of the Camry design. Since M2 and the Camry design both have the same magnet content, M2 further demonstrates the effectiveness of the proposed technique at reducing pulsating torque and such improvement is not just because of the reduction of PMs.

TABLE VI
PERFORMANCE COMPARISONS (BASED ON 3-D FE RESULTS)

	Camry	M1	M2
Torque [Nm][%]	231 (100)	210 (91)	234 (101)
PM mass [g][%]	923 (100)	729 (79)	914 (99)
PMUF [Nm/kg][%]	250 (100)	288 (115)	256 (102)
Back-EMF THD [%][%]	17 (100)	7 (41)	6 (35)
Cogging torque [Nm][%]	0.79 (100)	0.39 (49)	0.51 (65)
Pulsating torque [Nm][%]	41.6 (100)	19.2 (46)	18.6 (45)
Torque ripple ratio [%][%]	18 (100)	9 (50)	8 (44)

TABLE VII
EFFICIENCY COMPARISONS

	Camry	M1	M2
Current per phase rms [A]	195 (100)	195 (100)	195 (100)
Rotor mech. speed [r/min]	2800 (100)	3080 (110)	2800 (100)
Output power [kW][%]	68 (100)	68 (100)	69 (101)
Copper loss [kW][%]	3.9 (100)	3.9 (100)	3.9 (100)
Core loss [W][%]	448 (100)	464 (104)	416 (93)
Windage loss [W][%]	96 (100)	128 (133)	96 (100)
Efficiency [%][%]	93.8 (100)	93.8 (100)	94.0 (100.3)

TABLE VIII
PULSATING TORQUE COMPARISON AT DIFFERENT LOADS

	Camry	M1	M2
$I = 1.50 \text{ pu}$ [Nm][%]	60.5 (100)	27.4 (45)	26.4 (44)
$I = 1.00 \text{ pu}$ [Nm][%]	41.6 (100)	19.2 (46)	18.6 (45)
$I = 0.50 \text{ pu}$ [Nm][%]	18.9 (100)	9.9 (52)	9.7 (51)
$I = 0.25 \text{ pu}$ [Nm][%]	10.1 (100)	7.6 (75)	7.0 (69)

For the efficiency comparison in Table VII, the rated speed of M1 should be slightly increased since its voltage is reduced at the original speed. At the new speed, M1 produces the same output power as the Camry model. Although the core loss and windage loss of M1 are slightly elevated due to the increased speed, it still achieves about the same efficiency as the Camry model. M2 has the highest efficiency. Its flux density is more sinusoidally distributed in the stator core, resulting in less eddy current loss, and therefore, smaller core loss.

VII. PULSATING TORQUES AT DIFFERENT LOADS

In this section, the proposed designs are driven by different currents in order to investigate the pulsating torque reduction at different loads. All the machines are tuned to MTPA at the rated speed for each loading. The total instantaneous torques of M1, M2, and Camry are shown in Fig. 18 and their peak to peak pulsating torques are summarized in Table VIII.

The proposed designs show pulsating torque reduction across all the loadings. Particularly at overload ($I = 1.5 \text{ pu}$) or rated load ($I = 1 \text{ pu}$), the reduction is very prominent. The magnitude of ripple decreases as the loading decreases, as clearly demonstrated in Fig. 18. The reduction also decreases at very light loads ($I = 0.25 \text{ pu}$). However, the magnitude of the pulsating torque at light loads is much smaller than at rated load, so the

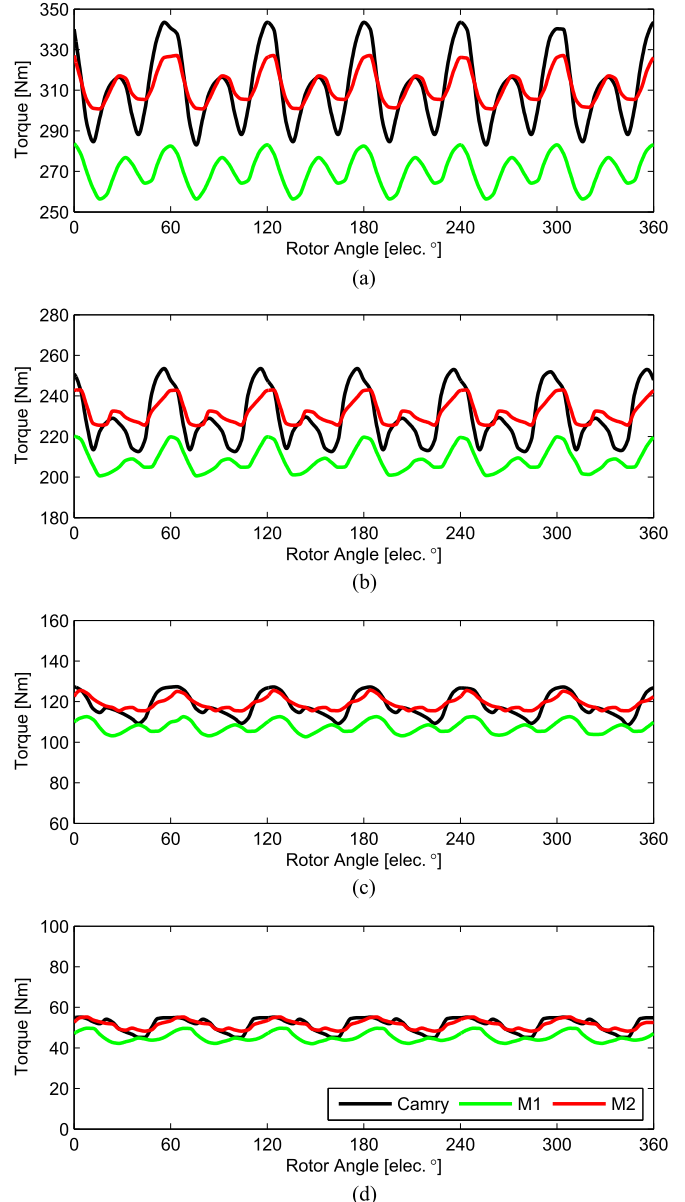


Fig. 18. Instantaneous torque of Camry, M1, and M2 at different loads: (a) overload $I = 1.50 \text{ pu}$; (b) rated load $I = 1.00 \text{ pu}$; (c) light load $I = 0.50 \text{ pu}$; and (d) very light load $I = 0.25 \text{ pu}$.

pulsating torque should not be an issue under a very-light-load condition.

VIII. CONCLUSION

A new design concept for IPMMs is proposed in this paper. The design concept uses a small number of rotor segments with different pitches of PMs and rotor notches arranged in the axial direction. The proposed design M1 is an optimum at which the utilization of rare earth materials and torque ripple are both reduced with a small amount of torque density reduction. Since the amount of PM material reduction is larger than that of the torque reduction, the torque per magnet weight (i.e., PMUF) is increased. The improved PMUF suggests that the rare earth PM materials are more efficiently used in the pro-

posed design M1. M1 still delivers the same power density and has about the same efficiency as the Camry design at a slightly increased speed. M2 matches the average torque without saving any PM materials. It mainly emphasizes that the proposed technique is more effective for torque ripple reduction than the conventional pole shaping technique in V-shape IPMMs with flux concentration. The improvement is very significant when the machine is fully loaded even with saturation occurring in the stator back iron. Overall, the rare earth PM materials can be more efficiently used in the proposed design concept if a small torque density reduction can be tolerated in a given application. The proposed design concept is also highly desirable for applications in which torque ripple is a primary concern.

ACKNOWLEDGMENT

The authors would like to thank Infolytica for making their MagNet FE software available.

REFERENCES

- [1] I. Boldea, L. N. Tutelea, L. Parsa, and D. Dorrell, "Automotive electric propulsion systems with reduced or no permanent magnets: an overview," *IEEE Trans. Ind. Electron.*, vol. 61, no. 10, pp. 5696–5711, Oct. 2014.
- [2] M. Takeno, A. Chiba, N. Hoshi, S. Ogasawara, and M. Takemoto, "Power and efficiency measurements and design improvement of a 50 kW switched reluctance motor for hybrid electric vehicles," in *Proc. IEEE Energy Convers. Congr. Expo.*, Phoenix, AZ, USA, 2011, pp. 1495–1501.
- [3] S. Ooi, S. Morimoto, M. Sanada, and Y. Inoue, "Performance evaluation of a high-power-density PMA-SynRM with ferrite magnets," *IEEE Trans. Ind. Appl.*, vol. 49, no. 3, pp. 1308–1315, May/Jun. 2013.
- [4] T. M. Jahns and W. L. Soong, "Pulsating torque minimization techniques for permanent magnet AC motor drives—a review," *IEEE Trans. Ind. Electron.*, vol. 43, no. 2, pp. 321–330, Apr. 1996.
- [5] S. Han, T. M. Jahns, W. L. Soong, M. K. Guven, and M. S. Illindala, "Torque ripple reduction in interior permanent magnet synchronous machines using stators with odd number of slots per pole pair," *IEEE Trans. Energy Convers.*, vol. 25, no. 1, pp. 118–127, Mar. 2010.
- [6] W. Q. Chu and Z. Q. Zhu, "Investigation of torque ripples in permanent magnet synchronous machines with skewing," *IEEE Trans. Magn.*, vol. 49, no. 3, pp. 1211–1220, Mar. 2013.
- [7] S. A. Evans, "Salient pole shoe shapes of interior permanent magnet synchronous machines," in *Proc. 19th Int. Conf. Elect. Mach.*, Rome, Italy, 2010, pp. 1–6.
- [8] W. Zhao, T. A. Lipo, and B.-I. Kwon, "Material-efficient permanent-magnet shape for torque pulsation minimization in SPM motors for automotive applications," *IEEE Trans. Ind. Electron.*, vol. 61, no. 10, pp. 5779–5787, Oct. 2014.
- [9] N. Bianchi, S. Bolognani, D. Bon, and M. Dai Pré, "Torque harmonic compensation in a synchronous reluctance motor," *IEEE Trans. Energy Convers.*, vol. 23, no. 2, pp. 466–473, Jun. 2008.
- [10] N. Bianchi, S. Bolognani, D. Bon, and M. Dai Pré, "Rotor flux-barrier design for torque ripple reduction in synchronous reluctance and PM-Assisted synchronous reluctance motors," *IEEE Trans. Ind. Appl.*, vol. 45, no. 3, pp. 921–928, May/Jun. 2009.
- [11] Z. S. Du and T. A. Lipo, "Improved use of rare earth permanent magnet materials and reduction of torque pulsation in interior permanent magnet machines," in *Proc. IEEE Energy Convers. Congr. Expo.*, Montreal, Canada, 2015, pp. 1773–1780.
- [12] M. Olszewski *et al.*, "Evaluation of the 2007 Toyota Camry hybrid synergy drive system," U.S. Department of Energy, Washington, DC, USA, 2008.
- [13] S. Williamson, T. J. Flack, and A. F. Volschenk, "Representation of skew in time-stepped two-dimensional finite-element models of electrical machines," *IEEE Trans. Ind. Appl.*, vol. 31, no. 5, pp. 1009–1015, Sep./Oct. 1995.
- [14] G. Y. Sizov, P. Zhang, D. M. Ionel, N. A. O. Demerdash, and M. Rosu, "Automated multi-objective design optimization of PM AC machines using computationally efficient FEA and differential evolution," *IEEE Trans. Ind. Appl.*, vol. 49, no. 5, pp. 2086–2096, Sep./Oct. 2013.
- [15] K. V. Price, R. M. Storn, and J. A. Lampinen, *Differential Evolution—A Practical Approach to Global Optimization*. Berlin, Germany: Springer-Verlag, 2005.
- [16] N. Bianchi and S. Bolognani, "Design techniques for reducing the cogging torque in surface-mounted PM motors," *IEEE Trans. Ind. Appl.*, vol. 38, no. 5, pp. 1259–1265, Sep./Oct. 2002.



Zhentao S. Du (S'16) received the B.E. degree in electrical engineering (first class Hons.) from the University of Technology, Sydney, Australia, in 2008, and the M.S. degree in electrical engineering from the University of Wisconsin–Madison, Madison, WI, USA, in 2013, where he is currently working toward the Ph.D. degree in electrical engineering in the Department of Electrical and Computer Engineering.

From 2009 to 2011, he was an Electrical Engineer in the Power and Energy Division, AECOM, Sydney. Since 2012, he has been a Research Assistant with the Wisconsin Electric Machines and Power Electronics Consortium, University of Wisconsin–Madison. His research interests include the analysis and design of electric machines and drives. He has several journal and conference publications, and has a U.S. patent.



Thomas A. Lipo (M'64–SM'71–F'87–LF'00) was born in Milwaukee, WI, USA. He received the B.E.E. and M.S.E.E. degrees from Marquette University, Milwaukee, in 1962 and 1964, respectively, and the Ph.D. degree in electrical engineering from the University of Wisconsin–Madison, Madison, WI, in 1968.

From 1969 to 1979, he was an Electrical Engineer in the Power Electronics Laboratory, Corporate Research and Development, General Electric Company, Schenectady, NY, USA. He became a Professor of electrical engineering at Purdue University, West Lafayette, IN, USA, in 1979, and in 1981, he joined the University of Wisconsin–Madison, where he served for 28 years as the W. W. Grainger Professor for power electronics and electrical machines. He is currently an Emeritus Professor with the University of Wisconsin–Madison and a Research Professor with Florida State University, Tallahassee, FL, USA.

Dr. Lipo received the Outstanding Achievement Award from the IEEE Industry Applications Society, the William E. Newell Award from the IEEE Power Electronics Society, and the 1995 Nicola Tesla IEEE Field Award from the IEEE Power Engineering Society. In 2002, he was elected a Member of the Royal Academy of Engineering, U.K.; in 2008, a member of the National Academy of Engineering, USA; and in 2013, a member of the National Academy of Inventors, USA. In 2014, he was selected to receive the IEEE Medal for Power Engineering. For the past 50 years, he has served the IEEE in numerous capacities, including as President of the IEEE Industry Applications Society in 1994.